

Diffusion Model as a Noise-Aware Latent Reward Model for Step-Level Preference Optimization

Tao Zhang^{1,3} Cheng Da² Kun Ding¹ Kun Jin² Yan Li² Tingting Gao² Di Zhang²
 Shiming Xiang^{1,3} Chunhong Pan¹
¹MAIS, CASIA ²Kuaishou Technology ³School of Artificial Intelligence, UCAS

Abstract

Preference optimization for diffusion models aims to align them with human preferences for images. Previous methods typically leverage Vision-Language Models (VLMs) as pixel-level reward models to approximate human preferences. However, when used for step-level preference optimization, these models face challenges in handling noisy images of different timesteps and require complex transformations into pixel space. In this work, we demonstrate that diffusion models are inherently well-suited for step-level reward modeling in the latent space, as they can naturally extract features from noisy latent images. Accordingly, we propose the **Latent Reward Model (LRM)**, which repurposes components of diffusion models to predict preferences of latent images at various timesteps. Building on LRM, we introduce **Latent Preference Optimization (LPO)**, a method designed for step-level preference optimization directly in the latent space. Experimental results indicate that LPO not only significantly enhances performance in aligning diffusion models with general, aesthetic, and text-image alignment preferences, but also achieves 2.5-28 \times training speedup compared to existing preference optimization methods. Our code and models are available at <https://github.com/Kwai-Kolors/LPO>.

1. Introduction

Diffusion models (Esser et al., 2024) have achieved significant success in the domain of text-to-image generation. Inspired by advancements in preference optimization (Touvron et al., 2023; Dubey et al., 2024) for Large Language Models (LLMs), several methods are proposed to align the diffusion model with human preferences. Diffusion-DPO (Wallace et al., 2024) extends Direct Preference Optimiza-

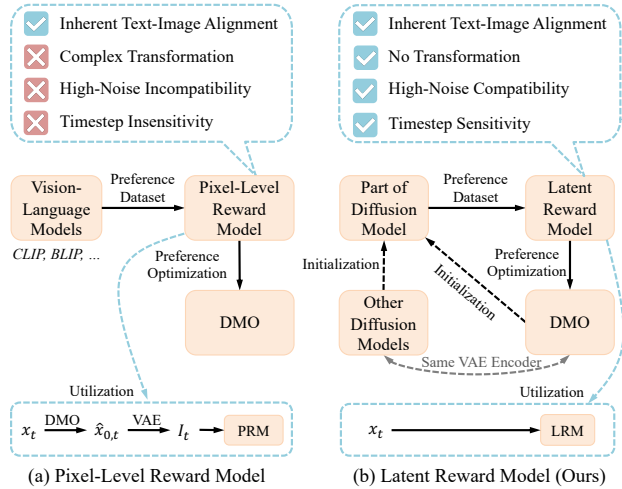


Figure 1. The comparison between the pixel-level reward model (a) and latent reward model (b) in step-level preference optimization. DMO denotes the diffusion model to be optimized.

tion (DPO) (Rafailov et al., 2023) to diffusion models, leveraging human-annotated data for training without requiring a reward model. However, the reliance on offline sampling introduces a distribution discrepancy between the preference data and the diffusion model, resulting in reduced optimization efficiency and effectiveness. DDPO (Black et al., 2024) and D3PO (Yang et al., 2024) employ online sampling and reward models for preference assessment. These methods typically assume that the preference order or reward value remains constant across all timesteps; however, this assumption may not hold in practice. To address this limitation, Step-by-step Preference Optimization (SPO) (Liang et al., 2024) introduces the Step-aware Preference Model (SPM) to predict preferences for different steps. Consequently, SPO can align models with aesthetic preference through step-level online sampling and preference assignment.

The reward models used in the aforementioned methods are mainly implemented by fine-tuning Vision-Language Models (VLMs) like CLIP (Radford et al., 2021) on preference datasets. We designate these models as Pixel-level Reward Models (PRMs) since they exclusively accept pixel-level image inputs. When applied to step-level preference

[✉] Corresponding author: Kun Ding <kun.ding@ia.ac.cn>.

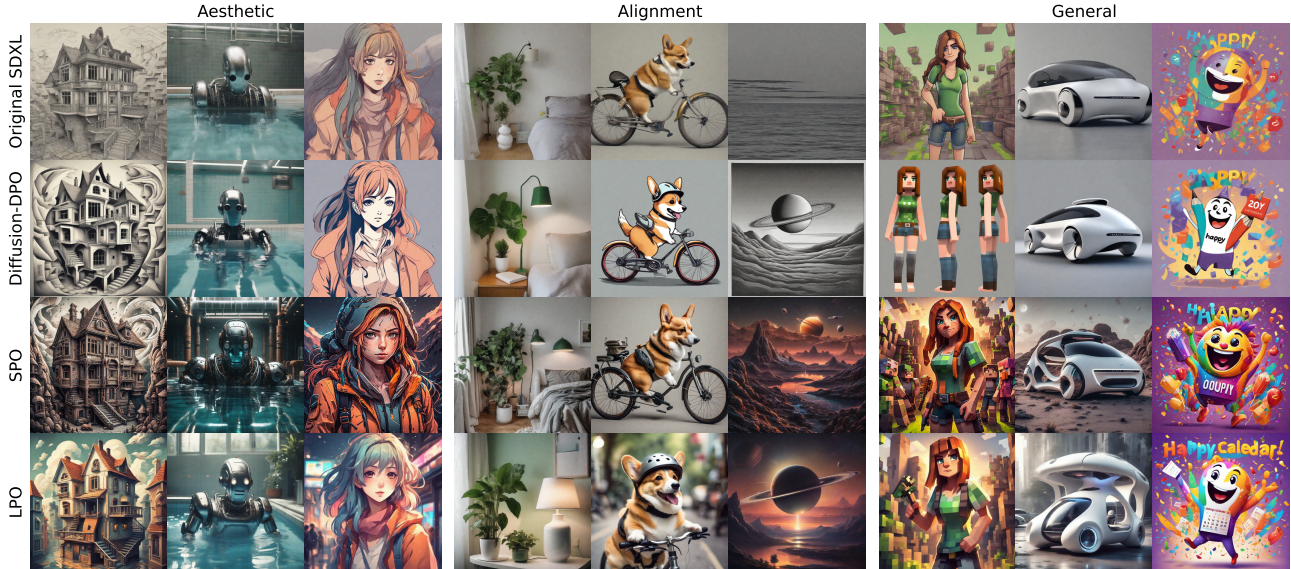


Figure 2. Qualitative comparison among different preference optimization methods based on SDXL (Podell et al., 2023). LPO excels in both aesthetics and text-image alignment, resulting in improved overall quality. Larger versions are provided in Fig. 12 and Fig. 13.

optimization, PRMs encounter several common challenges. (1) **Complex Transformation**: At each timestep t , they necessitate additional processes of diffusion denoising and VAE (Kingma, 2013) decoding to transform noisy latent images x_t into clean ones $\hat{x}_{0,t}$ and pixel-level images I_t . This results in an overly lengthy inference process, as illustrated in Fig. 1 (a) and Fig. 3 (a). (2) **High-Noise Incompatibility**: At large timesteps characterized by high noise, the predicted images I_t are significantly blurred, leading to a severe distribution shift from the training data of VLMs, *i.e.* clear images. Consequently, the predictions of PRMs are unreliable at large timesteps. (3) **Timestep Insensitivity**: PRMs exhibit limited sensitivity to variations across different timesteps since they usually do not include timesteps as input, complicating the understanding of how different timesteps influence image assessment. These issues hinder the effectiveness of PRMs for step-level reward modeling.

Is there a reward model that can naturally capture human preferences directly in the latent space while being aware of timesteps and compatible with high noise? In this paper, we find that the pre-trained diffusion model for text-to-image generation is an ideal choice because it exhibits several favorable characteristics, as listed in Fig. 1 (b). (1) It possesses inherent text-image alignment capabilities, owing to the pre-training on large-scale text-image pairs. (2) It can directly accept noisy latent images x_t without requiring additional diffusion forwarding and VAE decoding. (3) It is high-noise-compatible since it can extract features from x_t with various noise intensities, as is done during pre-training. (4) It naturally exhibits a strong sensitivity to timesteps, enabling it to effectively grasp the model’s attention at different timesteps. These pre-trained abilities make the diffusion

model particularly suitable for step-level reward modeling.

Based on the above insights, we propose using the diffusion model as a noise-aware **Latent Reward Model (LRM)**. For noisy latent images x_t , LRM utilizes visual features from the UNet (Ronneberger et al., 2015) and textual features from the text encoder to predict step-level preference labels. We further introduce the Visual Feature Enhancement (VFE) module to enhance LRM’s focus on the text-image alignment. To address the inconsistent preference issue in LRM’s training data, we propose the Multi-Preference Consistent Filtering (MPCF) strategy to ensure that winning images consistently outperform losing ones across multiple preference dimensions, thus enabling LRM to effectively learn human preferences. Finally, we employ LRM for step-level preference optimization, leading to a simple yet effective method termed **Latent Preference Optimization (LPO)**, where all steps are conducted within the latent space of diffusion models. Extensive experiments demonstrate that LPO significantly improves the image quality of various diffusion models and consistently outperforms existing DPO and SPO methods across the general, aesthetic, and alignment preferences, as indicated in Fig. 2. Moreover, LPO exhibits remarkable training efficiency, achieving a speedup of 10-28 \times over Diffusion-DPO and 2.5-3.5 \times over SPO.

2. Related Work

Reward Models for Human Preferences. Evaluating text-to-image generative models is a challenging problem. Several methods leverage Vision-Language Models (VLMs) to assess the alignment of generated images with human preferences. PickScore (Kirstain et al., 2023), HPSv2 (Wu

et al., 2023), and ImageReward (Xu et al., 2023) aim to predict general preference by fine-tuning CLIP (Radford et al., 2021) or BLIP (Li et al., 2022) on preference datasets. Zhang et al. (2024) proposes CLIP-based MPS to capture multiple preference dimensions. Black et al. (2024) and Jiang et al. (2024) utilize LLaVA (Liu et al., 2023) and BLIP, respectively, to improve the text-image alignment of generative models. Liang et al. (2024) introduces SPM, based on PickScore, to predict step-level preference labels during the denoising process. These reward models, limited to accepting pixel-level images, often face problems like distribution shift and cumbersome inference. In contrast, our proposed LRM can effectively address these issues. To the best of our knowledge, we are the first to employ diffusion models themselves for reward modeling.

Preference Optimization for Diffusion Models. Motivated by improvements in Reinforcement Learning from Human Feedback (RLHF) in LLMs (Touvron et al., 2023; Dubey et al., 2024), several preference optimization approaches for diffusion models have been proposed. Differentiable reward fine-tuning methods (Clark et al., 2024; Wu et al., 2025) directly adjust diffusion models to maximize the reward of generated images. However, they are susceptible to reward hacking issues and require gradient backpropagation through multiple denoising steps, significantly increasing the computation burden. DPOK (Fan et al., 2023) and DDPO (Black et al., 2024) formulate the denoising process as a Markov decision process and employ Reinforcement Learning (RL) techniques to align models with specific preferences. Nonetheless, they exhibit inferior performance on open vocabulary sets. Diffusion-DPO (Wallace et al., 2024) and D3PO (Yang et al., 2024) apply DPO (Rafailov et al., 2023) in LLMs to diffusion models, yielding better performance than the aforementioned RL-based methods. These methods optimize the trajectory-level preference; however, the preference order in intermediate steps may not be the same as that of the final generated images. In view of this, SPO (Liang et al., 2024) proposes a step-level preference optimization method. In this paper, our proposed LPO optimizes models in the latent space by employing the diffusion model as a powerful and cost-effective reward model, demonstrating significant effectiveness and efficiency.

3. Background

3.1. Latent Diffusion Models

The forward process of diffusion models gradually adds random Gaussian noise to clean latent images x_0 to obtain noisy latent images x_t , in the manner of a Markov chain:

$$q(x_t|x_{t-1}) = \mathcal{N}(\sqrt{\alpha_t}x_{t-1}, (1 - \alpha_t)\mathbf{I}), \quad (1)$$

where t is the timestep and $\mathcal{N}(\mu, \Sigma)$ denotes the Gaussian distribution. $\alpha_t = 1 - \beta_t$, where β_t is a pre-defined time-

dependent variance schedule. \mathbf{I} denotes the identity matrix. The backward process aims to denoise x_t , which can be formulated as follows according to DDIM (Song et al., 2021):

$$p_\theta(x_{t-1}|x_t) = \mathcal{N}(\mu_t, \sigma_t^2 \epsilon_t), \quad \epsilon_t \sim \mathcal{N}(\mathbf{0}, \mathbf{I}), \quad (2)$$

$$\mu_t = \sqrt{\bar{\alpha}_{t-1}}\hat{x}_{0,t} + \sqrt{1 - \bar{\alpha}_{t-1} - \sigma_t^2} \cdot \epsilon_\theta^{(t)}, \quad (3)$$

$$\hat{x}_{0,t} = \left(\frac{x_t - \sqrt{1 - \bar{\alpha}_t} \epsilon_\theta^{(t)}}{\sqrt{\bar{\alpha}_t}} \right), \quad (4)$$

$$\sigma_t = \eta \sqrt{(1 - \bar{\alpha}_{t-1}) / (1 - \bar{\alpha}_t)} \sqrt{1 - \alpha_t}, \quad (5)$$

where $\bar{\alpha}_t = \prod_{i=1}^t \alpha_i$ and $\eta \in [0, 1]$ is a hyperparameter to adjust the standard deviation σ_t . $\epsilon_\theta^{(t)}$ and $\hat{x}_{0,t}$ denote the noise and clean latent images predicted by diffusion models with parameters θ at timestep t .

3.2. Preference Optimization for Diffusion Models

Given winning latent images x_0^w , losing ones x_0^l , and condition c , Diffusion-DPO (Wallace et al., 2024) and D3PO (Yang et al., 2024) propagate the preference order of (x_0^w, x_0^l) to all denoising steps, thereby freely generating intermediate preference pairs (x_t^w, x_t^l) . They encourage models p_θ to generate x_t^w rather than x_t^l by minimizing

$$L_{DPO} = -\mathbb{E}_{\substack{x_{t,t+1}^w \sim p_\theta(x_{t,t+1}^w|x_0^w, c), \\ x_{t,t+1}^l \sim p_\theta(x_{t,t+1}^l|x_0^l, c)}} \left[\log \sigma \left(\beta \log \frac{p_\theta(x_t^w|x_{t+1}^w, c)}{p_{ref}(x_t^w|x_{t+1}^w, c)} - \beta \log \frac{p_\theta(x_t^l|x_{t+1}^l, c)}{p_{ref}(x_t^l|x_{t+1}^l, c)} \right) \right], \quad (6)$$

where β is a regularization hyperparameter and p_{ref} denotes the reference model, fixed to the initial value of p_θ .

However, the preference order along the denoising process is not always identical. Therefore, SPO (Liang et al., 2024) proposes SPM to predict preferences for intermediate steps, and sample the win-lose pairs (x_t^w, x_t^l) from the same x_{t+1} to make the two paths comparable. The optimization objective of SPO is to minimize

$$L_{SPO} = -\mathbb{E}_{x_t^w, x_t^l \sim p_\theta(x_t|x_{t+1}, c)} \left[\log \sigma \left(\beta \log \frac{p_\theta(x_t^w|x_{t+1}, c)}{p_{ref}(x_t^w|x_{t+1}, c)} - \beta \log \frac{p_\theta(x_t^l|x_{t+1}, c)}{p_{ref}(x_t^l|x_{t+1}, c)} \right) \right]. \quad (7)$$

As a Pixel-level Reward Model (PRM), SPM faces some common issues discussed in Sec. 1. First, as illustrated in Fig. 3 (a), it requires the forward of the diffusion model and VAE decoder. Second, it struggles to process highly blurred I_t when t is large. Third, although the AdaLN block (Peebles & Xie, 2023) is introduced in SPM to improve its sensitivity to timesteps, insufficient pre-training makes it challenging to understand the focus of different timesteps on image generation. These issues jointly diminish the effectiveness of SPM in step-level preference optimization.

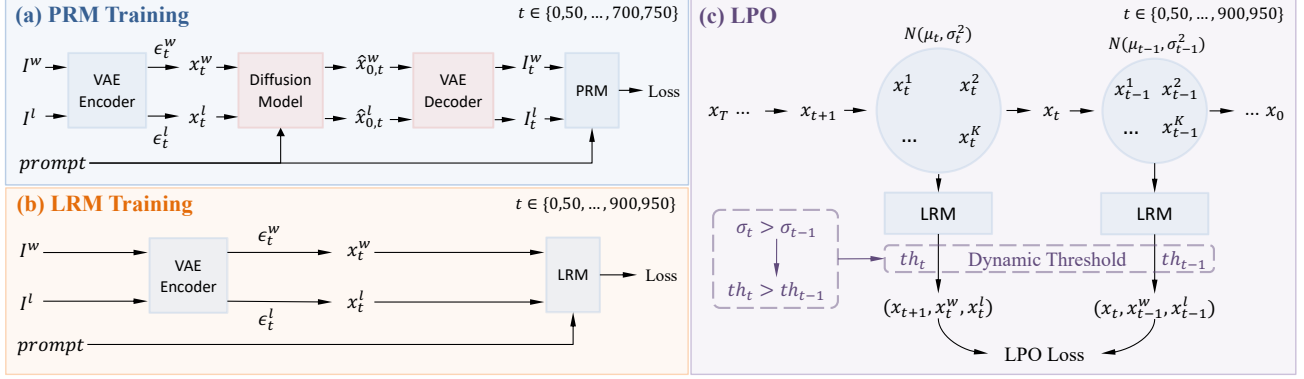


Figure 3. The training pipelines of PRM (a) and LRM (b) for step-level reward modeling, and LPO (c). Compared to PRM, LRM can directly process noisy latent images x_t . Therefore, LPO is able to perform sampling and training within the latent space.

4. Methodology

To address the limitations of PRMs, we propose the Latent Reward Model (LRM), which leverages diffusion models for reward modeling. To facilitate its training, we analyze the preference dataset and propose a Multi-Preference Consistent Filtering (MPCF) strategy. Finally, we introduce Latent Preference Optimization (LPO), a method that optimizes diffusion models in the latent space using LRM.

4.1. Latent Reward Model

As described in Sec. 1, the pre-trained diffusion model is remarkably suitable for step-level reward modeling due to its inherent ability to align texts and images, extract features directly from x_t at any timestep, and naturally accept timestep inputs. Therefore, we introduce the Latent Reward Model (LRM) to employ diffusion models for reward modeling.

Architecture of LRM. LRM leverages features of the UNet and text encoder in the diffusion model for preference prediction, as depicted in Fig. 4. Specifically, the textual features $f_p \in \mathbb{R}^{n_l \times n_p}$ are extracted from the prompt p by the text encoder, where n_l and n_p denotes the number of tokens and the dimension of textual features, respectively. Following CLIP (Radford et al., 2021), we use the last token $f_{eos} \in \mathbb{R}^{1 \times n_p}$ to represent the entire prompt and incorporate a text projection layer to obtain the final textual features $T \in \mathbb{R}^{1 \times n_d}$, where n_d represents the final dimension of textual and visual features. Each noisy latent image x_t is passed through the UNet to interact with textual features f_p . The visual features of UNet are averagedly pooled along the spatial dimension, resulting in the multiscale down-block features V_{down} and middle-block features V_{mid} as follows

$$V_{down}, V_{mid} = \text{AvgPool}(\text{UNet}(x_t, f_p)), \quad (8)$$

where $V_{down} = \{V_{d_i}, i = 1, \dots, L\}$. L is the number of down blocks and V_{d_i} represents features of the i -th down blocks. However, it is observed that these features lack sufficient correlations with the textual features. Inspired by

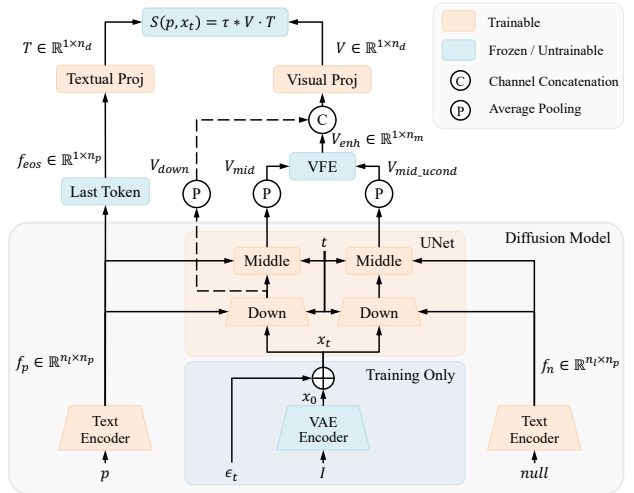


Figure 4. The architecture of LRM. The text encoder and UNet of diffusion models are utilized for preference prediction. The VAE encoder is only used in training.

the Classifier-Free Guidance (Ho & Salimans, 2022), we propose the **Visual Feature Enhancement (VFE)** module to enhance correlations between visual and textual features. It first extracts middle-block features $V_{mid.ucond}$ that are independent of textual information following a process similar to extracting V_{mid} , but with a null prompt. Then the enhanced visual features $V_{enh} \in \mathbb{R}^{1 \times n_m}$ can be calculated:

$$V_{enh} = V_{mid} + (gs - 1) * (V_{mid} - V_{mid.ucond}), \quad (9)$$

where $gs \geq 1$ is a hyperparameter and n_m denotes the dimension of V_{mid} . As gs increases, V_{mid} incorporates more features related to the text, leading to an enhanced focus on text-image alignment. When $gs = 1$, the VFE module is not utilized. Next, V_{enh} are concatenated with down-block features V_{down} along the channel dimension and projected into the final visual features $V \in \mathbb{R}^{1 \times n_d}$ by the visual projection layer. Finally, the preference score of x_t and p is computed as the dot product between textual and visual features after applying l_2 normalization:

$$S(p, x_t) = \tau * (l_2(V) \cdot l_2(T)), \quad (10)$$

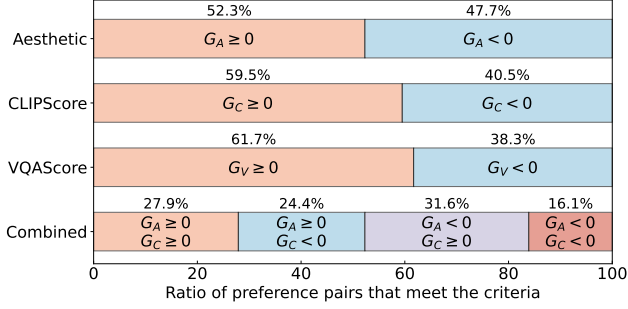


Figure 5. The distribution of preference score gaps in Pick-a-Pic.

where τ denotes the temperature coefficient following CLIP.

Training Loss. LRM is trained on the public preference dataset Pick-a-Pic v1 (Kirstain et al., 2023), denoted as D , which consists of triples (I^w, I^l, p) , each containing a preference image pair and a corresponding prompt. As depicted in Fig. 3 (b), given uniformly sampled timestep $t \sim \mathcal{U}(0, T)$ where T denotes the total denoising steps, we use the VAE encoder of the diffusion model to transform pixel-level images I into latent images x_0 , and then add x_0 with noise $\epsilon_t \sim \mathcal{N}(\mathbf{0}, \mathbf{I})$ to simulate x_t in the backward denoising process. Following the Bradley-Terry (BT) model (Bradley & Terry, 1952), the training loss of LRM is formulated as:

$$L_{LRM} = -\mathbb{E}_{t \sim \mathcal{U}(0, T), (I^w, I^l, p) \in D} \log \frac{e^{S(p, x_t^w)}}{e^{S(p, x_t^w)} + e^{S(p, x_t^l)}}, \quad (11)$$

$$x_t^* = \sqrt{\alpha_t} * \text{VAE}_{\text{encoder}}(I^*) + \sqrt{1 - \alpha_t} * \epsilon_t^*, \quad (12)$$

where $*$ $\in \{w, l\}$. During training, the parameters of VAE are frozen to ensure that the latent space of the LRM remains stable, while the text encoder and UNet are trainable.

4.2. Multi-Preference Consistent Filtering

Issue of Inconsistent Preferences. The training loss of LRM in Eqn. (11) involves the assumption that if x_0^w is preferred over x_0^l , then after adding noise of equal intensity, the preference order remains unchanged, meaning x_t^w continues to be preferred over x_t^l . However, this assumption breaks down when the winning image excels in one aspect but is inferior in other aspects. For example, if the winning image x_0^w has better details but exhibits weaker text-image alignment compared to the losing image x_0^l , the advantage in detail may be diminished after introducing significant noise, making the noisy losing image x_t^l potentially more preferred than x_t^w . Such situations frequently occur in the Pick-a-Pic (Kirstain et al., 2023) dataset. To demonstrate this, we employ the Aesthetic Score S_A (Schuhmann et al., 2022) to evaluate the aesthetic quality while using CLIP Score S_C (Radford et al., 2021) and VQAScore S_V (Lin et al., 2025) to assess the text-image alignment. Let $G_* = S_*(I^w) - S_*(I^l)$, $*$ $\in \{A, C, V\}$ denote the preference score gaps between winning and losing images. As illustrated in Fig. 5, nearly half of the winning images have

Table 1. Explored data filter strategies of Pick-a-Pic.

Part	Strategy	Filter Rule	Num
Win-Lose	1	$G_A \geq 0, G_C \geq 0, G_V \geq 0$	101,573
	2	$G_A \geq -0.5, G_C \geq 0, G_V \geq 0$	168,539
	3	$G_A \geq -1, G_C \geq 0, G_V \geq 0$	201,885
Tie	-	$ G_A \leq 0.2, G_C \leq 0.03, G_V \leq 0.07$	8,537

Aesthetic Scores lower than those of losing images. Similarly, around 40% of the winning images exhibit lower CLIP Scores and VQAScores. When considering both Aesthetic and CLIP scores, over 70% of the winning images score lower than the losing images in at least one aspect.

Multi-Preference Consistent Filtering. We hypothesize that if the winning image outperforms the losing image across various aspects, the preference order is more likely to remain consistent after introducing similar noise. Based on this hypothesis, we propose the Multi-Preference Consistent Filtering (MPCF) strategy, which aims to approximate the condition of the above hypothesis by filtering data using various preference score gaps. Pick-a-Pic v1 contains 511,840 win-lose pairs and 71,907 tie pairs. Three strategies are explored for win-lose pairs, as detailed in Tab. 1. The first strategy is the most strict, but it is observed that it causes the LRM to overfit to the aesthetic aspect while neglecting the text-image alignment. In contrast, the third strategy is the most lenient regarding aesthetics, resulting in the LRM being unable to perceive the aesthetics of the images. It is found that the second strategy effectively balances both aspects, leading us to choose it ultimately. Further investigations and experiments are detailed in Sec. 5.3.

4.3. Latent Preference Optimization

To utilize LRM for step-level preference optimization, we propose the Latent Preference Optimization (LPO) method.

Sampling and Training. As illustrated in Fig. 3 (c), at each timestep t , LPO samples a set of $x_t^i, i = 1, \dots, K$ from the same x_{t+1} . These noisy latent images are then directly fed into LRM to predict preference scores $S_t^i, i = 1, \dots, K$. The highest and lowest scores are normalized by the SoftMax function. If their score gap exceeds a predefined threshold th_t , the x_t with the highest score is selected as x_t^w , while the one with the lowest score is designated as x_t^l , forming a qualified training sample (x_{t+1}, x_t^w, x_t^l) . Finally, these samples are used to optimize the diffusion model, using the same loss with SPO, *i.e.* Eqn. (7). As a result, the entire process of LPO is performed within the latent space, eliminating the need to decode into pixel space, which significantly enhances the training efficiency of LPO.

Optimization Timesteps. Due to the inaccuracy of SPM at high-noise levels, SPO samples training data only at low to medium noise levels, specifically when $t \in [0, 750]$. In contrast, owing to the noise-aware capability of LRM, LPO

is able to collect training samples throughout the entire denoising process, covering $t \in [0, 950]$. Experiments in Sec. 5.3 demonstrate that training samples collected at high noise levels play a crucial role in preference optimization.

Dynamic Threshold. The sampling threshold th is a crucial hyperparameter in LPO. A higher threshold tends to sample win-lose pairs with more pronounced differences, improving the quality of the training samples but reducing their overall quantity. Conversely, a lower threshold increases the number of training samples but may introduce a certain amount of noisy samples. Given that the standard deviation σ_t in Eqn. (2) decreases with t , using a constant threshold across all timesteps can hinder the training effectiveness. To handle this, we implement a dynamic threshold strategy, which sets lower thresholds for smaller timesteps, as follows:

$$th_t = \frac{\sigma_t - \sigma_{min}}{\sigma_{max} - \sigma_{min}} * (th_{max} - th_{min}) + th_{min}, \quad (13)$$

where σ_{max} and σ_{min} are the maximum and minimum values of σ_t . The hyperparameters th_{max} and th_{min} are used to adjust the range of thresholds.

Selection of LRM in LPO. To avoid confusion, we refer to the diffusion model optimized in LPO as DMO. Since LPO is performed within the latent space, which is determined by the VAE encoder, the VAE of LRM should be identical to that of DMO. Therefore, the specific architecture of LRM can be initialized from DMO or any other diffusion models that share the same VAE encoder with DMO, as depicted in Fig. 1 (b). The former is termed *homogeneous optimization* because LRM and DMO share the same architecture, whereas the latter is called *heterogeneous optimization*.

5. Experiments

5.1. Experimental Setup

The experiments are mainly conducted on SD1.5 (Rombach et al., 2022) and SDXL (Podell et al., 2023) without refiner. The LRM is first trained on Pick-a-Pic and then used to fine-tune diffusion models through LPO. Unless otherwise specified, we employ *homogeneous optimization*.

LRM Training. We denote the LRM based on SD1.5 and SDXL as LRM-1.5 and LRM-XL, respectively. They are trained on the filtered Pick-a-Pic v1 (Kirstain et al., 2023) as clarified in Sec. 4.2. The gs in the VFE module is set to 7.5. More details are in Appendix A.

LPO Training. The same 4k prompts in SPO are used for the LPO training, randomly sampled from the training set of Pick-a-Pic v1. The DDIM scheduler (Song et al., 2021) with 20 inference steps is employed. We use all steps for sampling and training, *i.e.* $t \in [0, 50, \dots, 900, 950]$. The dynamic threshold range $[th_{min}, th_{max}]$ is set to $[0.35, 0.5]$ for SD1.5 and $[0.45, 0.6]$ for SDXL. The β in Eqn. (7) is set

Table 2. General and aesthetic preference scores on Pick-a-Pic validation unique set. * denotes the metrics are copied from (Liang et al., 2024). Others are evaluated using the official model.

Method	PickScore	ImageReward	HPSv2	HPSv2.1	Aesthetic
SD1.5					
Original	20.56	0.0076	26.46	24.05	5.468
*DDPO	21.06	0.0817	-	24.91	5.591
*D3PO	20.76	-0.1235	-	23.97	5.527
Diff.-DPO	20.99	0.3020	27.03	25.54	5.595
SPO	21.22	0.1678	26.73	25.83	5.927
LPO	21.69	0.6588	27.64	27.86	5.945
SDXL					
Original	21.65	0.4780	27.06	26.05	5.920
Diff.-DPO	22.22	0.8527	28.10	28.47	5.939
MaPO	21.89	0.7660	27.61	27.44	6.095
SPO	22.70	0.9951	28.42	31.15	6.343
LPO	22.86	1.2166	28.96	31.89	6.360

to 500 and the K in the sampling process is set to 4. Further details can be found in Appendix A.

Baseline Methods. We compare LPO with DDPO (Black et al., 2024), D3PO (Yang et al., 2024), Diffusion-DPO (Wallace et al., 2024), MaPO (Hong et al., 2024), and SPO (Liang et al., 2024). These methods are trained on similar datasets, such as Pick-a-Pic v1 and v2, to ensure a fair comparison. Details are provided in Appendix A.

Evaluation Protocol. We evaluate various diffusion models across three dimensions: general preference, aesthetic preference, and text-image alignment. The PickScore (Kirstain et al., 2023), HPSv2 (Wu et al., 2023), HPSv2.1 (Wu et al., 2023), and ImageReward (Xu et al., 2023) are utilized to assess the general preference. The aesthetic preference is evaluated using the Aesthetic Score (Schuhmann et al., 2022). Consistent with (Liang et al., 2024), both general and aesthetic preferences are assessed on the validation unique split of Pick-a-Pic v1, which has 500 different prompts. For text-image alignment, we employ the GenEval (Ghosh et al., 2023) and T2I-CompBench++ (Huang et al., 2023) metrics. All images are generated using the DDIM scheduler with 20 steps. Additionally, to assess the correlations between the LRM and aesthetics as well as text-image alignment, we propose two corresponding metrics. Specifically, we calculate the score gaps G_* , $*$ $\in \{A, C, L\}$ between winning and losing images, where A, C, L represent Aesthetic, CLIP, and LRM. For LRM, the score is taken at $t = 0$. Then the Pearson Correlation Coefficient (Pearson, 1896) between G_L and G_A is referred to as *Aes-Corr* while that between G_L and G_C is termed *CLIP-Corr*. They are evaluated on the validation unique and test unique splits of Pick-a-Pic v1.

5.2. Main Results

Quantitative Comparison. As indicated in Tab. 2, Tab. 3, and Tab. 4, Diffusion-DPO excels in enhancing the text-image alignment, while SPO focuses more on aesthetics. LPO outperforms both methods across three dimensions,

Table 3. Quantitative results on T2I-CompBench++ (Huang et al., 2023).

Model	Method	Color	Shape	Texture	2D-Spatial	3D-Spatial	Numeracy	Non-Spatial	Complex
SD1.5	Original (Rombach et al., 2022)	0.3783	0.3616	0.4172	0.1230	0.2967	0.4485	0.3104	0.2999
	Diff.-DPO (Wallace et al., 2024)	0.4090	0.3664	0.4253	0.1336	0.3124	0.4543	0.3115	0.3042
	SPO (Liang et al., 2024)	0.4112	0.4019	0.4044	0.1301	0.2909	0.4372	0.3008	0.2988
	LPO	0.5042	0.4522	0.5259	0.1928	0.3562	0.4845	0.3110	0.3308
SDXL	Original (Podell et al., 2023)	0.5833	0.4782	0.5211	0.1936	0.3319	0.4874	0.3137	0.3327
	Diff.-DPO (Wallace et al., 2024)	0.6941	0.5311	0.6127	0.2153	0.3686	0.5304	0.3178	0.3525
	MaPO (Hong et al., 2024)	0.6090	0.5043	0.5485	0.1964	0.3473	0.5015	0.3154	0.3229
	SPO (Liang et al., 2024)	0.6410	0.4999	0.5551	0.2096	0.3629	0.4931	0.3098	0.3467
LPO	0.7351	0.5463	0.6606	0.2414	0.4075	0.5493	0.3152	0.3801	

Table 4. Quantitative results on GenEval (Ghosh et al., 2023).

Model	Method	Single Object	Two Object	Counting	Colors	Position	Color Attribution	Overall
SD1.5	Original	97.50	37.12	34.69	75.53	3.75	6.75	42.56
	Diff.-DPO	98.44	38.38	36.25	77.93	4.50	7.25	43.79
	SPO	95.00	33.84	32.50	69.95	4.25	7.25	40.46
	LPO	97.81	54.80	40.94	79.52	7.00	10.25	48.39
SDXL	Original	93.75	63.38	30.94	80.05	9.25	19.00	49.40
	Diff.-DPO	99.06	76.52	45.00	88.83	11.50	25.75	57.78
	MaPO	95.63	68.94	32.19	83.51	11.50	17.75	51.59
	SPO	94.38	69.44	31.88	81.65	10.25	15.50	50.52
LPO	99.69	81.57	43.75	89.10	14.00	27.50	59.27	

Table 5. Comparisons of training speed.

Method	Reward Modeling	Preference Optimization	Total ↓ (A100 h)
SD1.5			
Diff.-DPO	0	240	240
SPO	32	48	80
LPO	15	8	23
SDXL			
Diff.-DPO	0	2,560	2,560
SPO	116	118	234
LPO	52	40	92

Table 6. Heterogeneous optimization based on LRM-SD1.5. P-S and I-R denote the PickScore and ImageReward metrics.

Model	Method	Aesthetic	GenEval	P-S	I-R	HPSv2	HPSv2.1
SD2.1 (Same VAE)	Original	5.673	48.59	20.92	0.3063	27.05	25.49
	LPO	5.969	56.01	21.76	0.7978	28.05	28.61
SDXL (Diff. VAE)	Original	5.920	49.40	21.65	0.4780	27.06	26.05
	LPO	5.953	40.85	20.82	0.3919	27.10	26.69

achieving higher Aesthetic Scores and superior performance on T2I-CompBench++ and GenEval metrics, leading to improved general preference scores. The user study results indicate similar findings, as discussed in Appendix B. Notably, the LPO-optimized SD1.5 even exhibits performance comparable to the original SDXL model across various metrics. We further validate the effectiveness of *heterogeneous optimization* in Tab. 6. SD1.5 and SD2.1 (Rombach et al., 2022) share the same VAE encoder, but SD1.5 has a smaller text encoder. Remarkably, fine-tuning SD2.1 using LRM-1.5 still yields significant improvements across various aspects, demonstrating that a smaller and inferior diffusion model can effectively fine-tune a larger and more advanced model as long as they share the same VAE encoder. In contrast, applying LRM-1.5 for the LPO of SDXL is ineffective due to the distribution mismatch in their latent spaces, which arises from differences in their VAE encoders.

Qualitative Comparison. The qualitative comparisons of various methods are illustrated in Fig. 2 and Fig. 11-Fig. 15. The images generated by Diffusion-DPO exhibit deficiencies in color and detail, whereas those produced by SPO demonstrate lower semantic relevance. Additionally, SPO’s excessive focus on aesthetics may lead to an overabundance

of details in some images, making them appear cluttered. In contrast, the images produced by LPO achieve a strong balance between text-image alignment and aesthetic quality, delivering a higher overall image quality.

Training Efficiency Comparison. LPO achieves significantly faster training speed. As shown in Tab. 5, considering the time required for both reward modeling and preference optimization, LPO requires only 23 A100 hours for SD1.5—just 1/10 of the training time needed for Diffusion-DPO and 1/3.5 of that for SPO. For SDXL, LPO’s training time is reduced to 1/28 and 1/2.5 of that for Diffusion-DPO and SPO, respectively. This efficiency is primarily due to LPO performing reward modeling and preference optimization directly in the latent space, avoiding the additional computational overhead of converting to pixel space.

5.3. Ablation Studies

If not specified, ablation experiments are conducted on SD1.5. Due to space limitations, we only use PickScore to reflect general preference in Tab. 7 and Tab. 8.

MPCF. As shown in Tab. 7, MPCF plays a critical role in LRM training. As discussed in Sec. 4.2, the inconsistent preference issue makes training on the full dataset (wo MPCF) ineffective, since it hinders the LRM from adequately focusing on aesthetics or text-image alignment, resulting in inferior LPO performance. On the other hand, different filtering strategies can profoundly impact the preference patterns of both the LRM and LPO-optimized models. The first filtering strategy strictly requires that winning

Table 7. Ablation results on MPCF of LRM’s training data. The second strategy balances aesthetics and alignment better.

Strategy	LRM		LPO		
	Aes-Corr	CLIP-Corr	Aesthetic	GenEval	PickScore
wo MPCF	0.1342	0.2274	5.772	45.66	21.49
1	0.4860	0.1011	6.390	45.77	<u>21.61</u>
2	0.1136	0.3588	<u>5.945</u>	<u>48.39</u>	21.69
3	-0.1152	0.4480	5.750	48.62	21.47

Table 8. Ablation results on the VFE module of LRM. Introducing VFE leads to better alignment and general preferences.

VFE	g_s	LRM		LPO		
		Aes-Corr	CLIP-Corr	Aesthetic	GenEval	PickScore
\times	1.0	0.1712	0.3211	6.053	46.60	21.51
\checkmark	3.0	0.1233	0.3441	5.923	47.35	21.53
\checkmark	7.5	0.1136	0.3588	<u>5.945</u>	48.39	21.69
\checkmark	10.0	0.1063	0.3592	5.937	<u>48.13</u>	<u>21.56</u>

images score higher than losing images across all aspects. However, since the diffusion model lacks explicit text-image alignment pre-training like CLIP, it is prone to overfitting to the visual features of the images, as indicated by a higher Aes-Corr. This overfitting results in reduced attention to alignment, as reflected by lower CLIP-Corr and GenEval scores. The second and third strategies relax the aesthetic constraints to varying degrees. However, excessively lenient constraints (the 3rd strategy) may cause LRM to focus solely on text-image alignment while neglecting image quality, resulting in a negative Aes-Corr. In contrast, the second strategy balances these two aspects better, leading to the highest general preference scores.

Structure of LRM. As illustrated in Tab. 8, the introduction of VFE ($g_s > 1$) leads to lower Aes-Corr values but higher CLIP-Corr values, indicating an enhanced emphasis on text-image alignment. This results in improvements in both the GenEval score and PickScore, with only a minor decline in the Aesthetic Score. As g_s increases, the LRM’s correlation with alignment steadily improves, while its correlation with aesthetics decreases. When g_s is set to 7.5, the model achieves the best overall performance.

Optimization Timesteps. Tab. 9 ablates different optimization timestep ranges, indicating that larger timesteps lead to better performance. The results achieved within the range of [750, 950] are nearly comparable to those achieved through optimization across the entire denoising process, *i.e.* [0, 950]. We suggest this is because diffusion models focus on low-frequency information, such as image layout and style, during larger timesteps, while emphasizing high-frequency texture details during smaller timesteps. The low-frequency components formed in higher timesteps play a decisive role in determining the overall quality of the generated images. This observation also demonstrates the effectiveness of LRM, even in very large timesteps. The qualitative

Table 9. Ablation results on optimization timestep ranges in LPO.

Range of t	Aesthetic	GenEval	P-S	I-R	HPSv2	HPSv2.1
[0, 200]	5.434	40.11	20.46	-0.0987	26.25	23.61
[250, 450]	5.527	43.00	20.76	0.1430	26.90	25.37
[500, 700]	5.742	44.44	20.95	0.1591	26.71	25.16
[750, 950]	<u>5.853</u>	<u>48.28</u>	<u>21.54</u>	<u>0.6337</u>	<u>27.47</u>	<u>27.64</u>
[0, 450]	5.573	42.71	20.63	0.0204	26.69	24.88
[0, 700]	5.765	44.93	21.02	0.3087	27.10	26.25
[0, 950]	5.945	48.39	21.69	0.6588	27.64	27.86

Table 10. Ablation results on different threshold strategies.

Threshold	Aesthetic	GenEval	P-S	I-R	HPSv2	HPSv2.1
0.3	5.853	46.75	21.22	0.5112	27.30	27.12
0.4	5.832	48.32	21.32	0.4789	27.08	26.37
0.5	5.900	48.39	21.57	0.6088	27.54	<u>27.42</u>
0.6	5.877	47.97	21.35	0.5510	27.25	26.73
[0.3, 0.45]	5.916	49.43	<u>21.58</u>	<u>0.6405</u>	<u>27.55</u>	27.33
[0.35, 0.5]	5.945	48.39	21.69	0.6588	27.64	27.86
[0.4, 0.55]	5.882	<u>48.77</u>	21.48	0.4791	27.30	27.13

comparison of different ranges is shown in Fig. 10.

Dynamic Sampling Threshold. The standard deviation σ_t of samples at smaller timesteps is relatively small according to the DDPM scheduling (Ho et al., 2020), making the constant threshold insufficient to accommodate all timesteps. As indicated in Tab. 10, the dynamic threshold strategy generally outperforms the constant threshold across different intervals, effectively alleviating this problem. We further explore other dynamic strategies in Appendix B.

6. Discussion and Conclusion

Conclusion. In this paper, we propose LRM to utilize diffusion models for step-level reward modeling, based on the insights that diffusion models possess text-image alignment abilities and can perceive noisy latent images across different timesteps. To facilitate the training of LRM, the MPCF strategy is introduced to address the inconsistent preference issue in LRM’s training data. We further propose LPO, a method that employs LRM for step-level preference optimization, operating entirely within the latent space. LPO not only significantly reduces training time but also delivers remarkable performance improvements across various evaluation dimensions, highlighting the effectiveness of employing the diffusion model itself to guide its preference optimization. We hope our findings can open new avenues for research in preference optimization for diffusion models and contribute to advancing the field of visual generation.

Limitations and Future Work. (1) The experiments in this work are conducted on UNet-based models and the DDPM scheduling method. Further research is needed to adapt these findings to larger DiT-based models (Esser et al., 2024) and flow matching methods (Lipman et al., 2023). (2) The Pick-a-Pic dataset mainly contains images generated

by SD1.5 and SDXL, which generally exhibit low image quality. Introducing higher-quality images is expected to enhance the generalization of the LRM. (3) As a step-level reward model, the LRM can be easily applied to reward fine-tuning methods (Prabhudesai et al., 2023; Clark et al., 2024), avoiding lengthy inference chain backpropagation and significantly accelerating the training speed. (4) The LRM can also extend the best-of-N approach to a step-level version, enabling exploration and selection at each step of image generation, thereby achieving inference-time optimization similar to GPT-o1 (gpt, 2024).

Impact Statement

This work introduces a preference optimization method used for text-to-image diffusion models. The method may have the following impacts:

- The reward model plays a crucial role in shaping the preferences of diffusion models. However, if the training data for the reward model contains biases, the optimized model may inherit or even amplify these biases, leading to the generation of stereotypical or discriminatory content about certain groups. To mitigate this risk, it is essential to ensure that the training data is diverse, representative, and fair.
- This method offers a way to enhance the quality of generated images in terms of aesthetics, relevance, and other aspects by leveraging a well-designed reward model. It can also be applied to safety domains, optimizing the model to prevent the generation of negative content.
- The optimized model can generate highly realistic images, which may be used to create misinformation or misleading content, thereby impacting public opinion and social trust. Therefore, it is essential to develop effective detection tools and mechanisms to identify synthetic content.

References

Learning to reason with llms. Technical report, OpenAI, 2024. URL <https://openai.com/index/learning-to-reason-with-llms/>.

Black, K., Janner, M., Du, Y., Kostrikov, I., and Levine, S. Training diffusion models with reinforcement learning. In *ICLR*, 2024.

Bradley, R. A. and Terry, M. E. Rank analysis of incomplete block designs: I. the method of paired comparisons. *Biometrika*, 39:324–345, 1952.

Cherti, M., Beaumont, R., Wightman, R., Wortsman, M., Ilharco, G., Gordon, C., Schuhmann, C., Schmidt, L., and Jitsev, J. Reproducible scaling laws for contrastive

language-image learning. In *CVPR*, pp. 2818–2829, 2023.

- Clark, K., Vicol, P., Swersky, K., and Fleet, D. J. Directly fine-tuning diffusion models on differentiable rewards. In *ICLR*, 2024.
- Dubey, A., Jauhri, A., Pandey, A., Kadian, A., Al-Dahle, A., Letman, A., Mathur, A., Schelten, A., Yang, A., Fan, A., et al. The llama 3 herd of models. *arXiv preprint arXiv:2407.21783*, 2024.
- Esser, P., Kulal, S., Blattmann, A., Entezari, R., Müller, J., Saini, H., Levi, Y., Lorenz, D., Sauer, A., Boesel, F., Podell, D., Dockhorn, T., English, Z., and Rombach, R. Scaling rectified flow transformers for high-resolution image synthesis. In *ICML*, 2024.
- Fan, Y., Watkins, O., Du, Y., Liu, H., Ryu, M., Boutilier, C., Abbeel, P., Ghavamzadeh, M., Lee, K., and Lee, K. DPOK: Reinforcement learning for fine-tuning text-to-image diffusion models. In *NeurIPS*, volume 36, pp. 79858–79885, 2023.
- Ghosh, D., Hajishirzi, H., and Schmidt, L. Geneval: An object-focused framework for evaluating text-to-image alignment. In *NeurIPS*, volume 36, pp. 52132–52152, 2023.
- Ho, J. and Salimans, T. Classifier-free diffusion guidance. *arXiv preprint arXiv:2207.12598*, 2022.
- Ho, J., Jain, A., and Abbeel, P. Denoising diffusion probabilistic models. In *NeurIPS*, volume 33, pp. 6840–6851, 2020.
- Hong, J., Paul, S., Lee, N., Rasul, K., Thorne, J., and Jeong, J. Margin-aware preference optimization for aligning diffusion models without reference. *arXiv preprint arXiv:2406.06424*, 2024.
- Hu, E. J., yelong shen, Wallis, P., Allen-Zhu, Z., Li, Y., Wang, S., Wang, L., and Chen, W. LoRA: Low-rank adaptation of large language models. In *ICLR*, 2022.
- Hu, X., Wang, R., Fang, Y., Fu, B., Cheng, P., and Yu, G. Ella: Equip diffusion models with llm for enhanced semantic alignment. *arXiv preprint arXiv:2403.05135*, 2024.
- Huang, K., Sun, K., Xie, E., Li, Z., and Liu, X. T2i-compbench: A comprehensive benchmark for open-world compositional text-to-image generation. In *NeurIPS*, volume 36, pp. 78723–78747, 2023.
- Jiang, D., Song, G., Wu, X., Zhang, R., Shen, D., Zong, Z., Liu, Y., and Li, H. CoMat: Aligning text-to-image diffusion model with image-to-text concept matching. *arXiv preprint arXiv:2404.03653*, 2024.

- Kingma, D. P. Auto-encoding variational bayes. *arXiv preprint arXiv:1312.6114*, 2013.
- Kirstain, Y., Polyak, A., Singer, U., Matiana, S., Penna, J., and Levy, O. Pick-a-Pic: An open dataset of user preferences for text-to-image generation. In Oh, A., Naumann, T., Globerson, A., Saenko, K., Hardt, M., and Levine, S. (eds.), *NeurIPS*, volume 36, pp. 36652–36663, 2023.
- Li, J., Li, D., Xiong, C., and Hoi, S. BLIP: Bootstrapping language-image pre-training for unified vision-language understanding and generation. In *ICML*, volume 162, pp. 12888–12900, 2022.
- Liang, Z., Yuan, Y., Gu, S., Chen, B., Hang, T., Cheng, M., Li, J., and Zheng, L. Aesthetic post-training diffusion models from generic preferences with step-by-step preference optimization. *arXiv preprint arXiv:2406.04314*, 2024.
- Lin, Z., Pathak, D., Li, B., Li, J., Xia, X., Neubig, G., Zhang, P., and Ramanan, D. Evaluating text-to-visual generation with image-to-text generation. In *ECCV*, pp. 366–384, 2025.
- Lipman, Y., Chen, R. T. Q., Ben-Hamu, H., Nickel, M., and Le, M. Flow matching for generative modeling. In *ICLR*, 2023.
- Liu, H., Li, C., Wu, Q., and Lee, Y. J. Visual instruction tuning. In Oh, A., Naumann, T., Globerson, A., Saenko, K., Hardt, M., and Levine, S. (eds.), *NeurIPS*, volume 36, pp. 34892–34916, 2023.
- Pearson, K. Mathematical contributions to the theory of evolution. iii. regression, heredity, and panmixia. *Philosophical Transactions of the Royal Society of London. Series A, Containing Papers of a Mathematical or Physical Character*, pp. 253–318, 1896.
- Peebles, W. and Xie, S. Scalable diffusion models with transformers. In *ICCV*, pp. 4195–4205, 2023.
- Podell, D., English, Z., Lacey, K., Blattmann, A., Dockhorn, T., Müller, J., Penna, J., and Rombach, R. SDXL: Improving latent diffusion models for high-resolution image synthesis. *arXiv preprint arXiv:2307.01952*, 2023.
- Prabhudesai, M., Goyal, A., Pathak, D., and Fragkiadaki, K. Aligning text-to-image diffusion models with reward backpropagation. *arXiv preprint arXiv:2310.03739*, 2023.
- Radford, A., Kim, J. W., Hallacy, C., Ramesh, A., Goh, G., Agarwal, S., Sastry, G., Askell, A., Mishkin, P., Clark, J., Krueger, G., and Sutskever, I. Learning transferable visual models from natural language supervision. In *ICML*, volume 139, pp. 8748–8763, 2021.
- Rafailov, R., Sharma, A., Mitchell, E., Manning, C. D., Ermon, S., and Finn, C. Direct preference optimization: Your language model is secretly a reward model. In *NeurIPS*, volume 36, pp. 53728–53741, 2023.
- Rombach, R., Blattmann, A., Lorenz, D., Esser, P., and Ommer, B. High-resolution image synthesis with latent diffusion models. In *CVPR*, pp. 10684–10695, 2022.
- Ronneberger, O., Fischer, P., and Brox, T. U-net: Convolutional networks for biomedical image segmentation. In *MICCAI*, pp. 234–241, 2015.
- Schuhmann, C., Beaumont, R., Vencu, R., Gordon, C., Wightman, R., Cherti, M., Coombes, T., Katta, A., Mullis, C., Wortsman, M., Schramowski, P., Kundurthy, S., Crowson, K., Schmidt, L., Kaczmarczyk, R., and Jitsev, J. LAION-5B: An open large-scale dataset for training next generation image-text models. In *NeurIPS*, volume 35, pp. 25278–25294, 2022.
- Song, J., Meng, C., and Ermon, S. Denoising diffusion implicit models. In *ICLR*, 2021.
- Touvron, H., Martin, L., Stone, K., Albert, P., Almahairi, A., Babaei, Y., Bashlykov, N., Batra, S., Bhargava, P., Bhosale, S., et al. Llama 2: Open foundation and fine-tuned chat models. *arXiv preprint arXiv:2307.09288*, 2023.
- Wallace, B., Dang, M., Rafailov, R., Zhou, L., Lou, A., Purushwalkam, S., Ermon, S., Xiong, C., Joty, S., and Naik, N. Diffusion model alignment using direct preference optimization. In *CVPR*, pp. 8228–8238, 2024.
- Wu, X., Hao, Y., Sun, K., Chen, Y., Zhu, F., Zhao, R., and Li, H. Human preference score v2: A solid benchmark for evaluating human preferences of text-to-image synthesis. *arXiv preprint arXiv:2306.09341*, 2023.
- Wu, X., Hao, Y., Zhang, M., Sun, K., Huang, Z., Song, G., Liu, Y., and Li, H. Deep reward supervisions for tuning text-to-image diffusion models. In *ECCV*, pp. 108–124, 2025.
- Xu, J., Liu, X., Wu, Y., Tong, Y., Li, Q., Ding, M., Tang, J., and Dong, Y. ImageReward: Learning and evaluating human preferences for text-to-image generation. In *NeurIPS*, volume 36, pp. 15903–15935, 2023.
- Yang, K., Tao, J., Lyu, J., Ge, C., Chen, J., Shen, W., Zhu, X., and Li, X. Using human feedback to fine-tune diffusion models without any reward model. In *CVPR*, pp. 8941–8951, 2024.
- Zhang, S., Wang, B., Wu, J., Li, Y., Gao, T., Zhang, D., and Wang, Z. Learning multi-dimensional human preference for text-to-image generation. In *CVPR*, pp. 8018–8027, 2024.

A. Experimental Details

LRM Training. We train LRM-1.5 for 4,000 steps with 500 warmup steps and LRM-XL for 8,000 steps with 1000 warmup steps, both using the learning rate 1e-5. The batch size is 128 for LRM-1.5 and 32 for LRM-XL, respectively. Following CLIP (Radford et al., 2021), the initial value of τ in Eqn (10) is set to $e^{2.6592}$. The training resolution is 512 for SD1.5 and 1024 for SDXL. For SDXL, which includes two text encoders, we utilize only the OpenCLIP ViT-bigG (Cherti et al., 2023) as the text encoder of LRM-XL.

LPO Training. Both SD1.5 and SDXL are fine-tuned for 5 epochs. Following SPO (Liang et al., 2024), we employ LoRA (Hu et al., 2022) to fine-tune models. The LoRA rank is 4 for SD1.5 and 64 for SDXL. All experiments are conducted on 4 A100 GPU. Other hyperparameters are provided in Tab. 11. The experimental setting of SD2.1 is the same as SD1.5.

Table 11. Hyperparameters of LPO training.

	SD1.5 (Rombach et al., 2022)	SDXL (Podell et al., 2023)
Learning Rate	5e-5	1e-5
LoRA Rank	4	64
β	500	500
K	4	4
Sampling Threshold Range	[0.35, 0.5]	[0.45, 0.6]
Sampling Batch Size	5	4
Training Resolution	512×512	1024×1024
Training Epoch	5	5
Training Batch Size	10	4

Baseline Methods. Specifically, SPO and LPO are trained on Pick-a-Pic v1 (Kirstain et al., 2023) while Diffusion-DPO and MaPO are trained on Pick-a-Pic v2 (Kirstain et al., 2023), an extended version of Pick-a-Pic v1. Pick-a-Pic v1 consists of 583,737 preference pairs, whereas Pick-a-Pic v2 contains over 950,000 pairs. In the practice of SPO, DDPO (Black et al., 2024) and D3PO (Yang et al., 2024) are reproduced on 4k prompts randomly sampled from Pick-a-Pic v1, which are the same as the training data used for SPO and LPO. Therefore, the comparison between these methods can be considered fair.

B. Additional Experiments

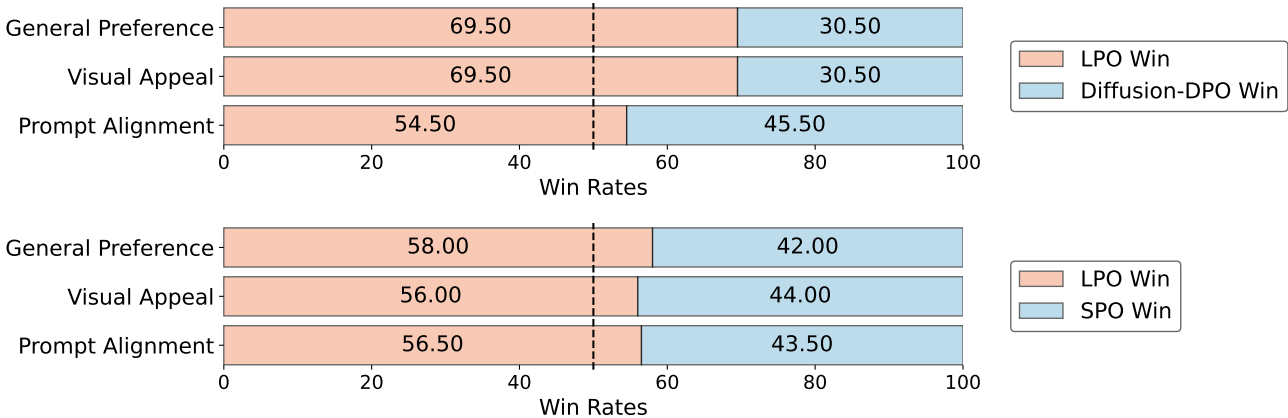


Figure 6. User study results on 200 prompts from HPSv2 benchmark (Wu et al., 2023) and DPG-Bench (Hu et al., 2024).

User Study. We conduct human evaluation experiments for LPO, SPO, and Diffusion-DPO. The evaluation set consists of 200 prompts, with 100 randomly sampled from HPSv2 benchmark (Wu et al., 2023) and 100 randomly sampled from DPG-Bench (Hu et al., 2024). For each prompt, the model generates four images. For each image, five expert evaluators score it across three dimensions: general preference, visual appeal, and prompt alignment. Subsequently, votes are cast to determine the winning relationships among the different models. The results are illustrated in Fig. 6. Similar to the results of automatic metrics in the main paper, LPO outperforms both SPO and Diffusion-DPO across three dimensions. Compared to T2I-CompBench and GenEval results, the advantage of LPO on text-image alignment in the human evaluation results is

not particularly pronounced. We believe this is because the prompts used for human evaluation are not specifically designed to assess text-image alignment, and different models exhibit relatively good alignment.

Table 12. The correlations of reward models with aesthetics and text-image alignment, along with the preference prediction accuracy on the validation and test set of Pick-a-Pic v1.

	Model	Aes-Corr	CLIP-Corr	VQA-Corr	Val-Test Accuracy
Specific Reward Model (VLM-Based)	Aesthetic (Schuhmann et al., 2022)	-	-	-	54.03
	CLIP Score (CLIP-H) (Radford et al., 2021)	-	-	-	61.84
	VQAScore (Lin et al., 2025)	-	-	-	59.16
General Reward Model (VLM-Based)	ImageReward (Xu et al., 2023)	0.108	0.425	0.417	62.66
	HPSv2 (Wu et al., 2023)	0.007	0.602	0.406	64.76
	HPSv2.1 (Wu et al., 2023)	0.191	0.432	0.332	65.58
	PickScore (Kirstain et al., 2023)	0.066	0.490	0.402	71.93
	Average	0.093	0.487	0.389	-
General Reward Model (Diffusion-Based)	LRM-1.5 ($t = 0$)	0.115	0.359	0.339	65.46
	LRM-1.5 ($t = 200$)	0.111	0.356	0.336	67.21
	LRM-XL ($t = 0$)	0.073	0.403	0.390	67.44
	LRM-XL ($t = 200$)	0.089	0.401	0.385	<u>69.31</u>

LRM as Pixel-Wise Reward Model. The LRM can also serve as a pixel-wise reward model when combined with the corresponding VAE encoder. Tab. 12 shows the correlations of different reward models with aesthetics and text-image alignment. Aes-Corr is employed to assess the correlation with aesthetics, while the CLIP-Corr and VQA-Corr are utilized to measure alignment correlation. The calculation method for VQA-Corr is similar to that of CLIP-Corr, as described in Sec. 5.1, with the CLIP Score replaced by VQAScore. It is observed that the LRMs, especially LRM-XL, exhibit aesthetic and alignment correlations comparable to those of VLM-based models, as indicated by similar Aes-Corr and VQA-Corr values. The CLIP-Corr of LRMs is slightly lower than the average value of VLM-based reward models, likely because VLM-based models are fine-tuned versions of CLIP (Radford et al., 2021) or BLIP (Li et al., 2022), leading to greater similarity to CLIP. The accuracy on the validation and test sets of Pick-a-Pic is also present in Tab. 12. LRMs demonstrate competitive performance, with larger models (LRM-XL) exhibiting higher accuracy. Moreover, we find that adding slight noise to the latent images ($t = 200$) can achieve better accuracy. This can be attributed to the fact that slight noise can better activate the feature extraction capabilities and improve the generalization of diffusion models.

Table 13. Ablation results on the hyperparameter β .

β	Aesthetic	GenEval	PickScore	ImageReward	HPSv2	HPSv2.1
20	5.920	46.95	21.53	0.6407	27.54	28.13
100	6.031	48.23	21.68	0.6443	27.47	27.52
500	5.945	48.39	21.69	0.6588	27.64	27.86
1000	5.858	48.44	21.39	0.4785	27.22	26.47
5000	5.647	43.87	20.95	0.2970	27.00	25.68

Regularization HyperParameter β . β is a regularization hyperparameter to control the deviation of the optimized model (p_θ in Eqn. (7)) with the reference model p_{ref} . As shown in Tab. 13, as β increases, the regularization effect becomes stronger, which slows down the model’s optimization speed and leads to poorer performance. Conversely, if β is too small ($\beta = 20$), the regularization constraint becomes too weak, potentially reducing the model’s generalization ability and decreasing the quality of the generated images. The performance is optimal when β is within the range of 100 to 500.

Table 14. Ablation results on the dynamic threshold strategies.

Strategy	Aesthetic	GenEval	PickScore	ImageReward	HPSv2	HPSv2.1
Standard Deviation	5.945	48.39	21.69	0.6588	27.64	27.86
Variance	5.921	47.78	21.57	0.5054	27.42	26.93
Timestep	5.929	48.22	21.65	0.6465	27.42	27.25

Other Dynamic Threshold Strategy. In the main paper, we dynamically correlate the threshold in LPO sampling with the standard deviation σ_t in DDPM (Ho et al., 2020). Here we explore alternative strategies. The first strategy involves

replacing σ_t with variance σ_t^2 . Consequently, the threshold can be formulated as:

$$th_t = \frac{\sigma_t^2 - \sigma_{min}^2}{\sigma_{max}^2 - \sigma_{min}^2} * (th_{max} - th_{min}) + th_{min}. \quad (14)$$

The second strategy is linearly correlating the threshold with the timestep t :

$$th_t = \frac{t - t_{min}}{t_{max} - t_{min}} * (th_{max} - th_{min}) + th_{min}, \quad (15)$$

where t_{min} and t_{max} denote the minimum and maximum optimization timesteps, respectively. The values of different strategies are illustrated in Fig. 7. The threshold range is $[0.35, 0.5]$ and the timestep range is $[0, 950]$. It can be observed that the standard deviation strategy sets higher thresholds for middle timesteps, while the variance strategy sets lower thresholds. As shown in Tab. 14, the standard deviation strategy achieves the best performance across various metrics. This may be because the standard deviation strategy better accommodates the variations between x_t at different timesteps.

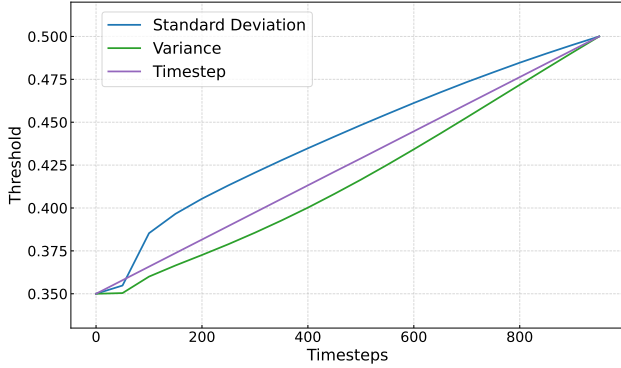


Figure 7. The thresholds of different strategies.

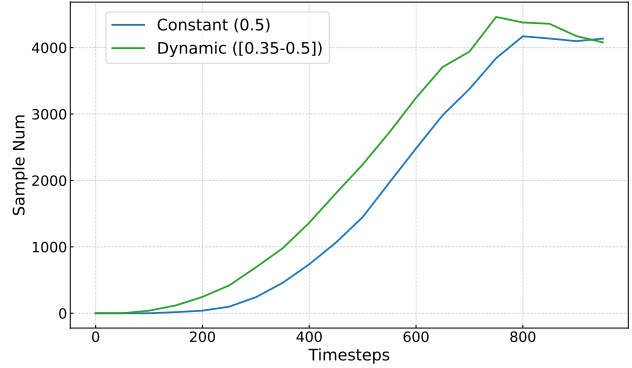


Figure 8. The number of valid samples of different timesteps .

Fig. 8 illustrates the number of valid samples of different timesteps for both constant and dynamic (standard deviation) threshold strategies. Dynamic threshold strategy significantly increases the number of valid samples, especially at intermediate timesteps.

C. Additional Visualizations

Predicted Images I_t at Different Timesteps. Fig. 9 illustrates the predicted images I_t generated through the diffusion forward and VAE decoding processes, as shown in Fig. 3 (a). As discussed in the main paper, predicted images at large timesteps tend to be very blurred, causing a significant distribution shift from the original images. This makes it challenging for PRMs to adapt to these blurred images without adequate pre-training and extensive datasets, resulting in unreliable predictions at large timesteps.

Optimization Timesteps. The generated images of different optimization timestep ranges are illustrated in Fig. 10. Larger timestep ranges result in more pronounced improvements in the quality of the generated images. We think there are two main reasons. Firstly, small timesteps in the denoising process primarily focus on high-frequency details, which do not lead to significant changes in the layout and style of the image. Secondly, as indicated in Fig. 8, the smaller the timestep, the fewer the valid samples, resulting in less optimization at the corresponding timesteps. Furthermore, compared to images in the range $[750, 950]$, those in $[0, 950]$ exhibit richer details, including both foreground and background, which also demonstrates that optimization at smaller timesteps aids in the enhancement of image details.

More Comparison. Fig. 11 presents the generated images of different methods based on SD1.5 (Rombach et al., 2022). Fig. 12 and Fig. 13 show the larger version of images in Fig. 2. Fig. 14 and Fig. 15 provide more generated images of various methods based on SDXL (Podell et al., 2023). Some keywords in prompts are emphasized using **bold** formatting.

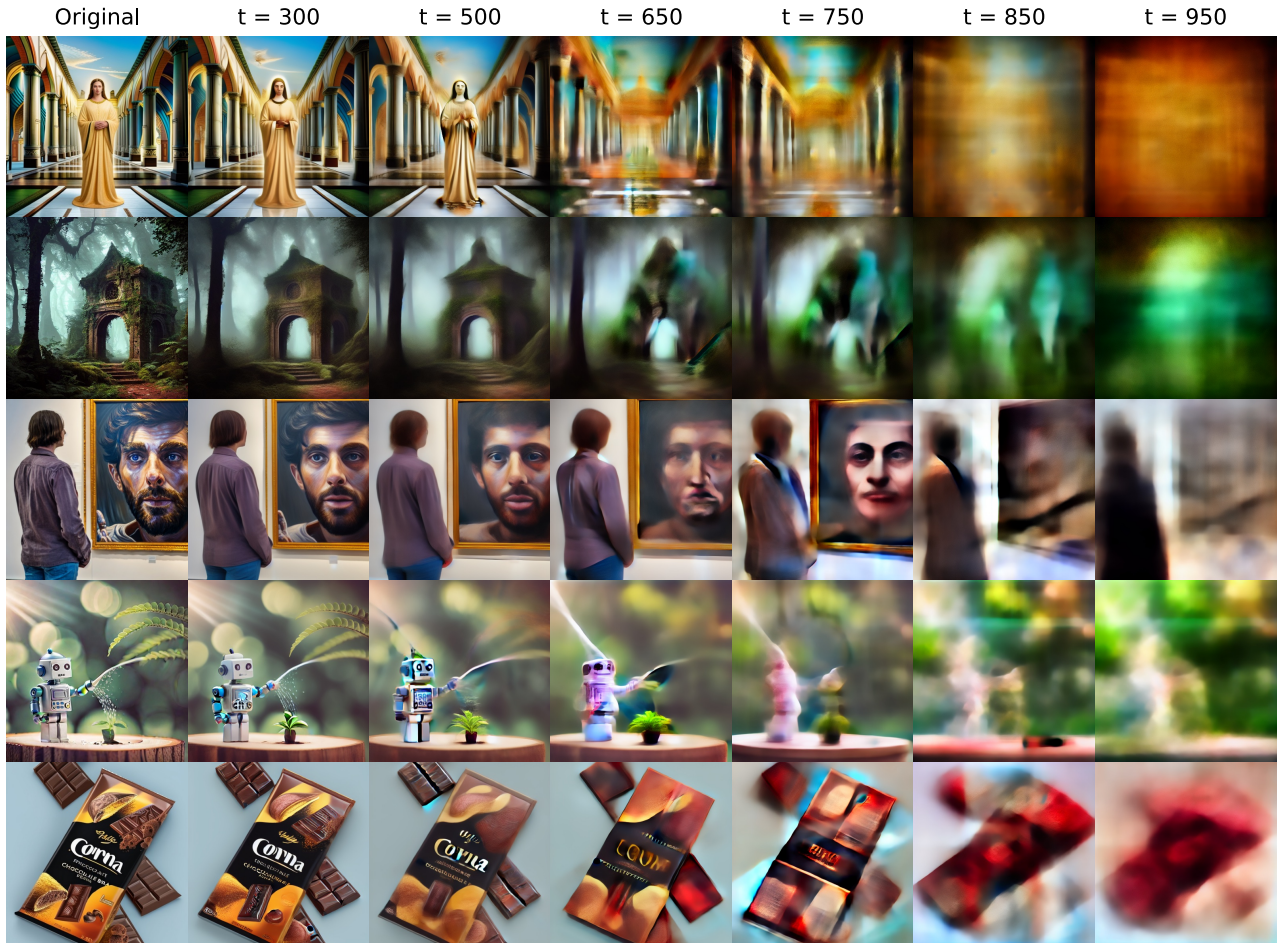


Figure 9. Predicted images I_t in Fig. 3 (a) at different timesteps. The original images come from the Pick-a-Pic v1 dataset (Kirstain et al., 2023).

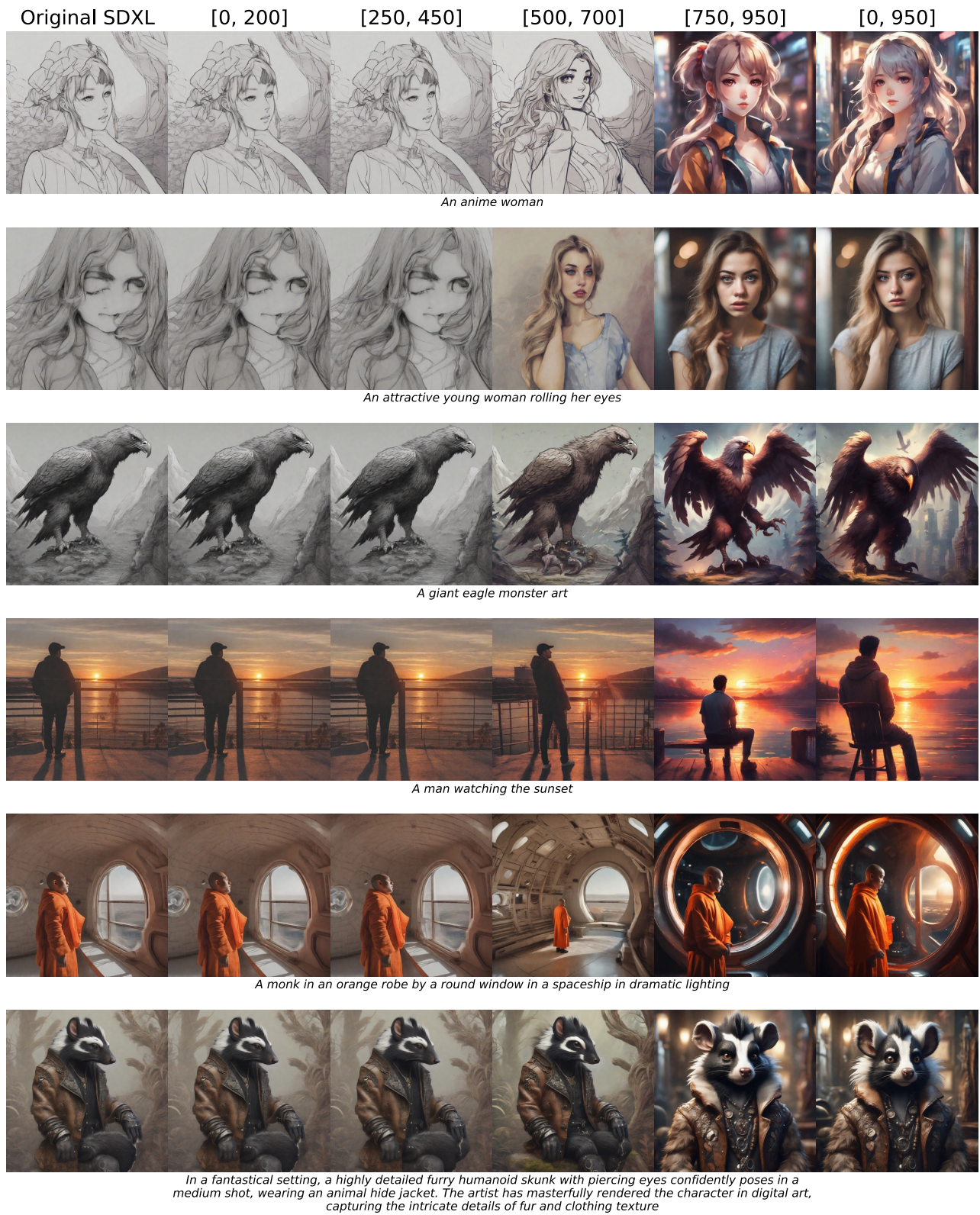


Figure 10. Qualitative comparison of various optimization timestep ranges based on SDXL.



a brown monkey with a **playful expression** wears a pair of aviator sunglasses as it swings through a lush jungle canopy. its tail curls around a vine, and the **sunlight reflects off its sunglasses**, capturing a sense of **adventure and fun**.



an oil painting depicts a **starry night** in the desert, with a red **astronaut** staring intently at a blue **astronaut** who clutches a knife. the vast desert stretches out before them, dunes rippling in the moonlight. the sky above is **filled with twinkling stars**, while the distant horizon glows faintly from the setting sun. the tension between the **two astronauts** is palpable, as if a dramatic confrontation is about to unfold.



Close-up portrait of middle-aged man, illuminated by soft natural light. His face is **deeply lined** and his eyes show emotion, **expressing sadness and contemplation**. Shot using an 85mm lens, the focus is on his facial features while **the background is softly blurred**. Soft lighting creates subtle highlights and shadows that accentuate the skin's texture.



A **dolphin jumping over a rowboat**

Figure 11. Qualitative comparison of various preference optimization methods based on SD1.5.

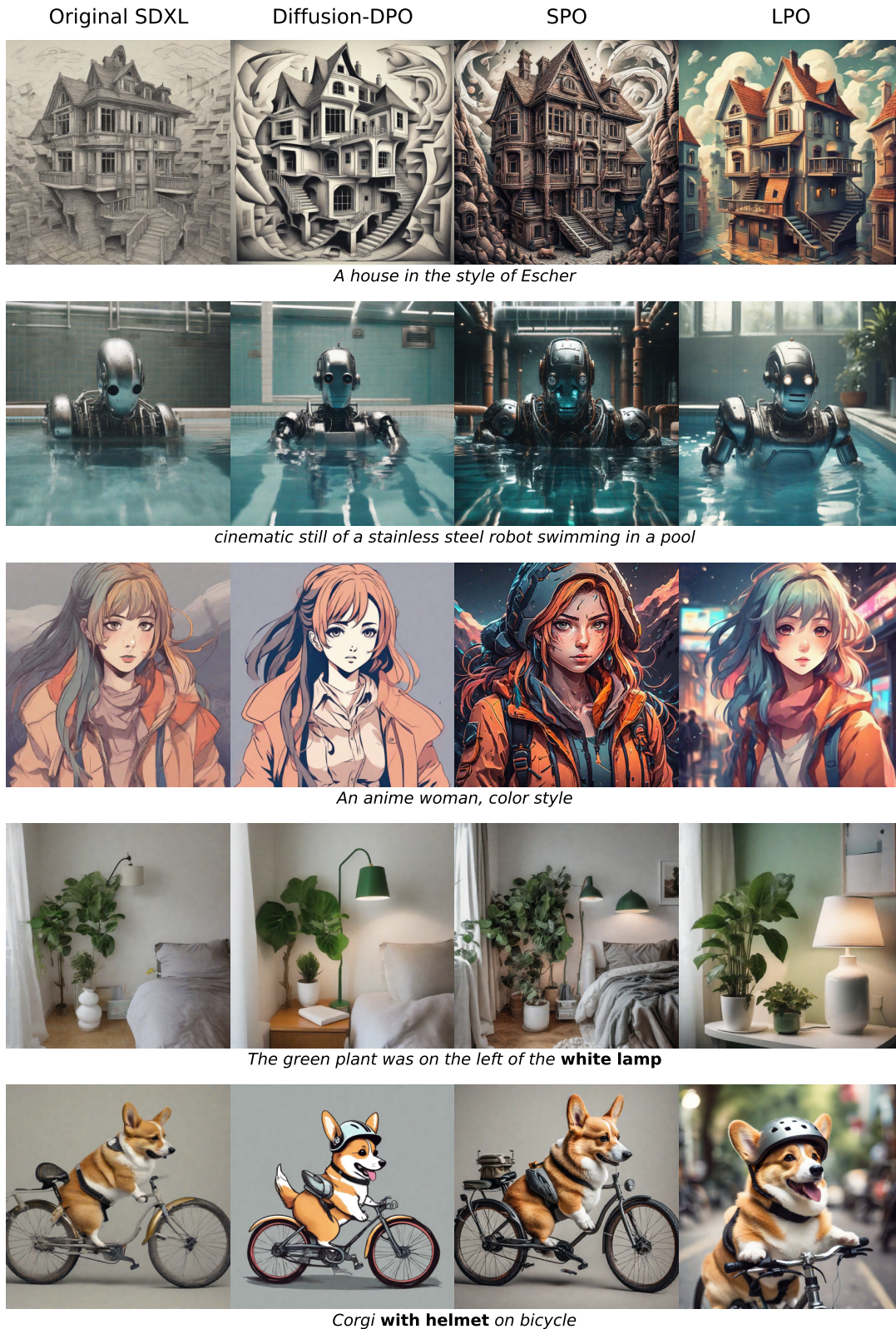


Figure 12. Qualitative comparison of various preference optimization methods based on SDXL.

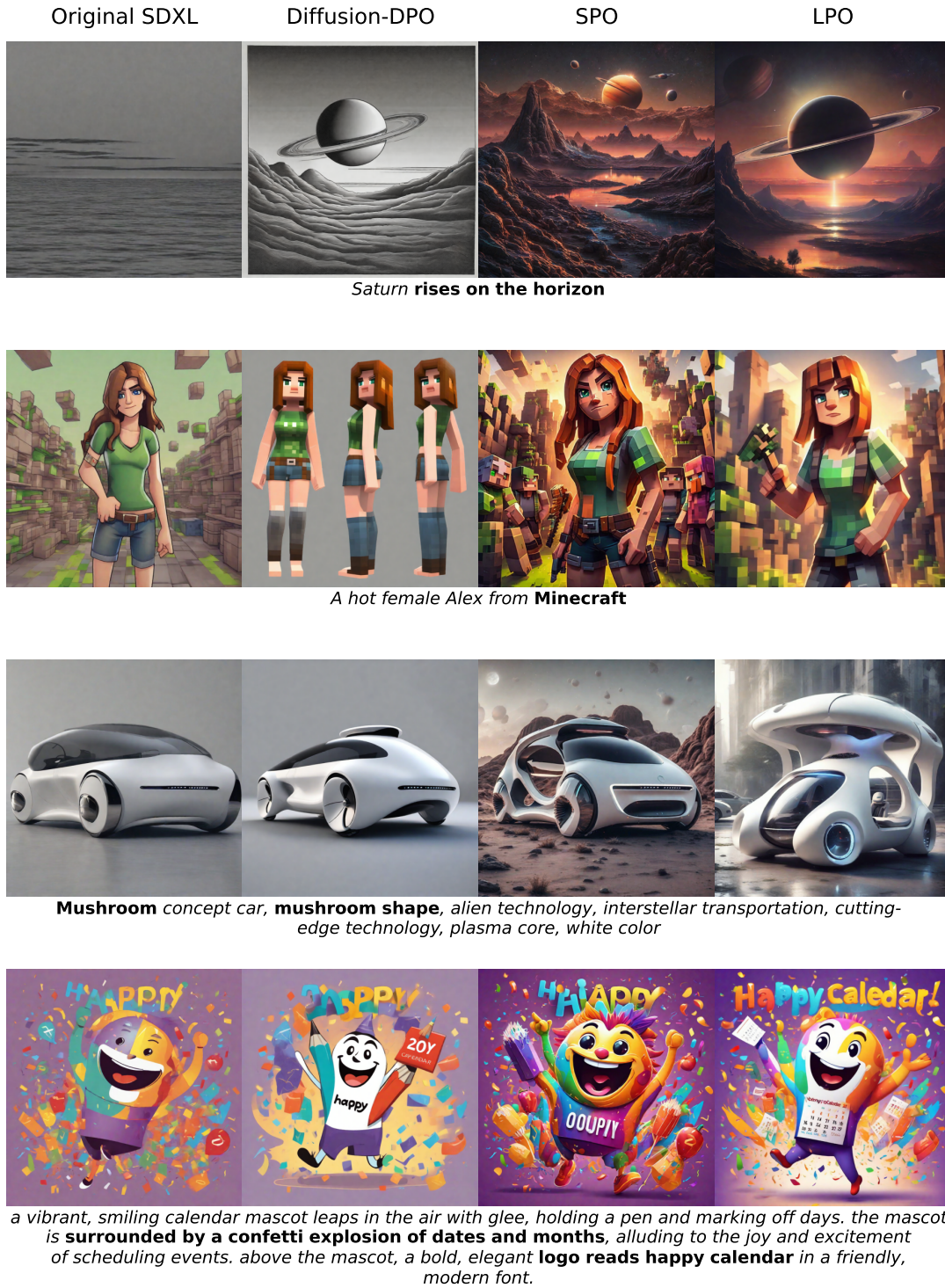


Figure 13. Qualitative comparison of various preference optimization methods based on SDXL.



Figure 14. Qualitative comparison of various preference optimization methods based on SDXL.



Giant Hello Kitty ice sculpture, crystal clear ice sculpture art, sitting posture showing the iconic bow, classic round face design including beard and round nose, finely carved fish patterns on the dress, and transparent geometric shape to create the image of the beloved character. Stepped ice base, winter park environment background, ground covered with snow, cloudy day with diffuse light, figures in front showing size proportions, transparent ice showing internal light refraction, professional photography perspective, ultra-high definition image quality, magnificent scale, Exquisite ice sculpture craftsmanship, winter festival atmosphere



A woman wearing an ultramarine jacket and yellow slacks, yellow socks and yellow shoes, wearing all black sunglasses, short wavy hair without bangs, holding a black dog with a blue leash in her hands, the dog in her Right, fashion model, red lipstick, on an asphalt road with a yellow line, single yellow background, oriental fusion clothing, low angle, like a fashion pictorial, concept art, decorative, hyper-detailed, realistic, bright colors, realistic, model posture



a weary unicorn grad student sits at a cluttered wooden desk, surrounded by stacks of books and papers. the dim light from a small desk lamp illuminates the room, casting shadows on the walls. dark circles are evident under the unicorn's eyes, as it holds a cup of coffee in one hoof, trying to stay awake while studying. the moonlight from the window reflects off its horn, adding a magical touch to the scene.



a detailed sketch of mario from the classic video game series is depicted on a textured parchment. he wears his signature red cap and overalls, white gloves, and holds a green turtle shell. the drawing captures his cheerful expression and iconic mustache, with fine pencil strokes adding depth and dimension.

Figure 15. Qualitative comparison of various preference optimization methods based on SDXL.